Discerning Between All Possible Activation Mechanisms of a Plasmon-Driven Chemical Reaction

Rifat Kamarudheen,[1,2,§] Guus J. W. Aalbers,[1,§] Ruben F. Hamans,[1,2,4§] Leon P. J. Kamp[3] and Andrea Baldi[1,2,4]*

[1]DIFFER - Dutch Institute for Fundamental Energy Research, De Zaale 20, 5612 AJ Eindhoven, The Netherlands

[2]Institute for Complex Molecular Systems and [3]Fluid Dynamics Laboratory, Department of Applied Physics, Eindhoven University of Technology, 5600 MB Eindhoven, The Netherlands

[4]Department of Physics and Astronomy, Vrije Universiteit Amsterdam, De Boelelaan 1081, 1081 HV Amsterdam, The Netherlands

[§]*These authors contributed equally to this work.*

*e-mail: a.baldi@vu.nl

ABSTRACT

Localized surface plasmon resonances (LSPRs) in metal nanoparticles can drive chemical reactions at their surface, but it is often challenging to disentangle the exact activation mechanism. The decay of LSPRs can lead to photothermal heating, electromagnetic hot spots, and the ejection of non-thermalized charge carriers, but all these processes typically occur simultaneously and on ultrafast timescales. Here, we develop a plasmon-assisted Au@Ag core@shell nanorod synthesis in which each plasmon-decay mechanism can be independently assessed. Using different illumination wavelengths combined with extinction spectroscopy, transmission electron microscopy, thermal characterization, and finite-difference time-domain simulations, we unequivocally identify interband holes as the main driving force behind the silver shell growth. Our conclusion is corroborated by single-particle studies on gold nanospheres that display isotropic reactivity, consistent with interband hole-driven nanoparticle syntheses. Our strategy to discern between plasmon-activation mechanisms can be extended to a variety of light-driven processes including photocatalysis, nanoparticle syntheses, and drug delivery.

TOC GRAPHICS

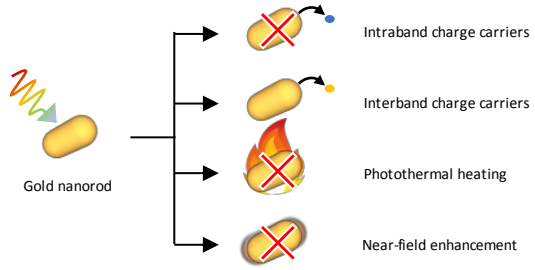

Understanding and engineering light-matter interactions is fundamental to a wide variety of photochemical processes from photovoltaics,[1] to (nano)lithography,[2] chemical sensing,[3] drug-delivery,[4] nanoparticle syntheses,[5] and heterogeneous photocatalysis.[6] For example, illumination of metal nanoparticles can tune their activity and selectivity towards industrially relevant catalytic processes, as demonstrated for the epoxidation of propylene on copper nanoparticles[7] and the hydrogenation of carbon dioxide on rhodium nanocubes.[8] Similarly, irradiation of gold and silver nanospheres can be used to photochemically transform them into larger anisotropic structures with very high yield.[9,10] These examples demonstrate how light can act as an ingredient to tailor and accelerate kinetically challenging multi-electron chemical reactions that are unattainable in the dark.[11]

Light-activated processes occurring on metal nanostructures are typically attributed to the excitation of localized surface plasmon resonances (LSPRs).[12] LSPRs are light-driven oscillations of free charge carriers in metal nanostructures that give rise to strong scattering and absorption.[13] Their radiative decay (scattering) generates intense electromagnetic fields at the vicinity of the nanoparticle surface, typically known as near-fields, which can activate photosensitive reactions.[14] On the other hand, the non-radiative decay (absorption) of LSPRs can drive chemical reactions *via* photothermal heating, that can accelerate temperature-sensitive

reactions according to the Arrhenius relation,[15] or *via* hot charge carriers generated by intraband[16] and interband transitions,[17–19] which can activate redox reactions. In most light-driven processes, however, it is often challenging to disentangle and quantify the relative contributions of these mechanisms[20–24] due to several factors, such as the extremely short lifetimes of hot charge carriers,[12] the low quantum efficiency of photochemical processes,[17] the similar linear power response of photochemical reactions to near-fields and hot charge carriers,[25] non-linear two photon[14] and two electron[11] processes, the typically complex light and heat transport in the reaction volume leading to both nanoscopic and macroscopic temperature rises,[20,26] and the simultaneous generation of interband and intraband carriers under visible light excitation in metals such as gold and copper.[19]

Here, we develop a light-driven Au@Ag core@shell nanorod (NR) synthesis in which each plasmon-activation mechanism can be independently assessed. We first characterize the silver shell growth rate and reaction evolution in the dark, using *in situ* extinction spectroscopy and transmission electron microscopy. We then compare the growth rate in the dark to the one measured under excitation of either the transverse or the longitudinal plasmon resonances of the gold nanorods, using a 532 nm or a 730 nm laser, respectively. The laser intensities in the two cases are tuned to obtain the same total amount of absorbed optical power in the reaction volume and therefore the same magnitude of photothermal effects. We find that the silver shell growth rate under excitation of the longitudinal resonance equals the one in the dark and therefore shows no plasmonic enhancement. On the other hand, excitation of the transverse resonance displays strongly enhanced reaction rates at the beginning of the reaction, and this enhancement drastically decreases as the silver shell approaches a thickness of about 4 nm. The striking rate disparity of silver shell growth under identical total absorbed optical power in 532 nm and 730

nm illumination demonstrates the non-thermal nature of the enhancement mechanism, which is later independently confirmed by direct thermal measurements and numerical calculations.

Furthermore, using finite-difference time-domain (FDTD) simulations, we show that the intensity of the near-fields increases with increasing silver shell thickness. As a consequence, near-field enhancements cannot explain the observed time evolution of the reaction rate when using 532 nm light. The absence of any rate enhancement under 730 nm irradiation, which corresponds to an energy just below the interband threshold of gold,[27] shows that low energy plasmonic intraband charge carriers do not contribute to the reaction. Under 532 nm irradiation of gold, however, most of the energy is used to generate hot interband holes,[19] suggesting they are the main contributor for the observed rate enhancement. Strikingly, these holes have typical mean free paths of a few nanometers,[28] corresponding to the silver shell thickness at which plasmon-driven effects are effectively quenched, thereby confirming our interpretation. Finally, we corroborate the nature of the hot charge carriers by monitoring the shell growth at the single-particle level using dark-field scattering spectroscopy. Here, we observe an isotropic nature of the silver shell growth under polarized laser irradiation and the quenching of laser-induced growth for shell thicknesses above 4 nm, in agreement with the interpretation of a predominant role of interband hot holes in our plasmon-driven chemical reaction.[29]

Silver shell growth in the dark

Gold nanorods with a length of 78 ± 10 nm and a diameter of 25 ± 5 nm are colloidally synthesized using a seed-mediated growth technique (see Methods and Supplementary S1).[30] We choose these nanorod dimensions so that we can excite both interband and intraband charge carriers when illuminating at their transverse resonance with a 532 nm laser ($\lambda_{transverse}$ = 514 nm),

while selectively exciting only intraband charge carriers while illuminating at their longitudinal resonance with a 730 nm laser ($\lambda_{longitudinal}$ = 744 nm) (Supplementary S1). No interband charge carriers can be generated in gold for excitation wavelengths above ~700 nm.[27]

To discriminate the mechanisms underlying our plasmon-driven chemistry, we use an Au@Ag core@shell nanorod synthesis adapted from a previously reported method.[20] Briefly, aqueous solutions of bis(p-sulphonatophenyl)phenylphosphine dihydrate dipotassium (BSPP), $AgNO_3$, and ascorbic acid are added to a gold nanorod suspension, to yield a final optical density of ~0.36 (see Methods and Figure 1a). The growth of the core@shell nanoparticle occurs *via* the reduction of Ag^+ to Ag^0 and the concomitant oxidation of ascorbic acid on the gold nanorod surface.[31] The Ag:BSPP ratio is tuned to 2.5, in order to slow down the silver shell growth in dark conditions. The suspension is kept in a temperature-controlled cuvette holder and is actively cooled to 6 °C using a water bath, along with magnetic stirring at 300 rpm.

We first perform the core@shell synthesis in the dark for 76 h and monitor the silver shell growth using transmission electron microscopy (TEM) and *in situ* extinction spectroscopy (Figure 1b and c). TEM images of the synthesis after 23 h show the growth of a ~1 nm conformal silver shell around the gold nanorods (Supplementary S1). This nanorod structure is henceforth referred to as NR_1, with NR_0 corresponding to the initial bare gold nanorods. The growth of a 1 nm conformal silver shell induces a blue shift of the longitudinal plasmon resonance of ~24 nm, as shown in Figure 1c. The initial conformal shell growth is followed by the formation of a cuboidal structure with sharp corners and a silver shell that reaches a thickness of about 4 nm after 46 h (NR_2). The formation of cuboidal nanorods is accompanied by a red shift of ~9 nm of their longitudinal plasmon resonance. Finally, over the course of 76 hours, the reaction proceeds further leading to even thicker and often asymmetric silver shells (NR_3), which

gives rise to a blue shift of the longitudinal plasmon resonance of ~30 nm. Our proposed correlation between the measured spectral changes and the morphology of the growing core@shell nanostructures identified by TEM measurements is consistent with the FDTD calculations (see Supplementary S1).

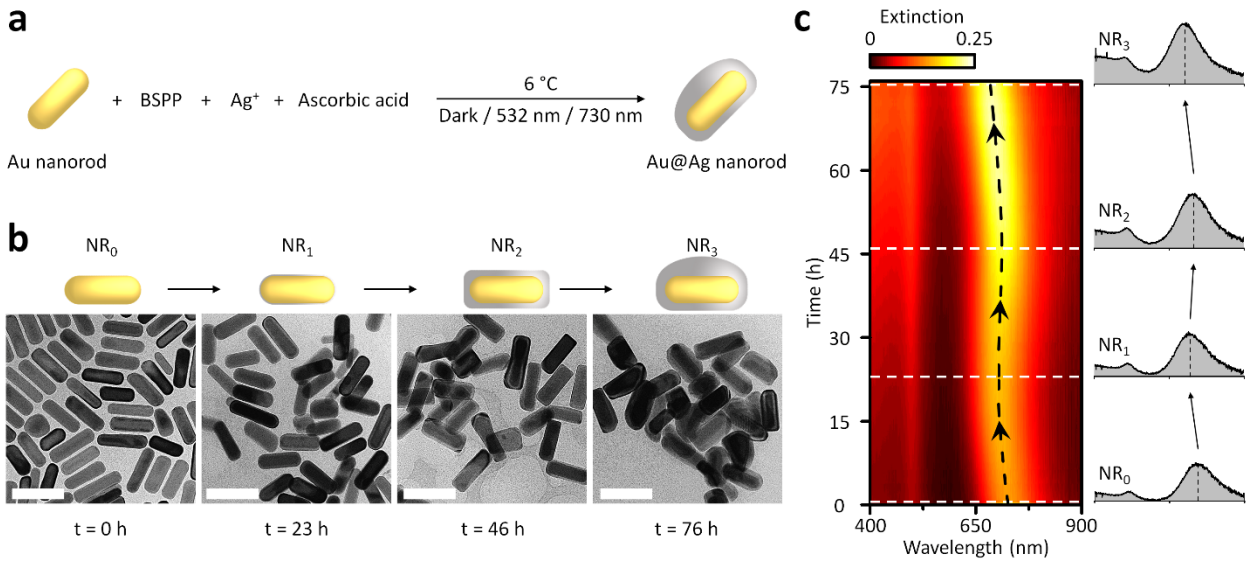

Figure 1. Core@shell growth in the dark. (**a**) Schematic representation of the Au@Ag core@shell nanorod synthesis. (**b**) TEM images and representative sketches of Au@Ag core@shell nanorods grown in dark conditions at times t = 0 h (NR_0), 23 h (NR_1), 46 h (NR_2), and 76 h (NR_3). The scale bars correspond to 100 nm. (**c**) Colormap of the time evolution of the extinction spectrum of the Au@Ag core@shell nanorod solution in the dark. The extinction spectra are measured through the 4 mm path length of the cuvette. White dashed lines correspond to the times at which TEM images are taken. The black dashed line indicates the shift in plasmon resonance with time.

Silver shell growth under plasmon excitation

After studying the silver shell growth dynamics and shape evolution in the dark, we repeat the synthesis under two different laser illumination conditions. In a 10 × 4 mm cuvette, a 500 μL nanorod growth mixture is illuminated using a 240 mW 532 nm or a 55 mW 730 nm continuous wave (cw) laser, in separate experiments. These laser powers are chosen so that the total optical power absorbed inside the reaction volume is the same in both irradiation experiments, as determined by modeling the photon propagation inside the nanorod suspension using Monte Carlo calculations (Supplementary S2).[26]

From our *in situ* extinction spectroscopic measurements during 24 hours of illumination with the 730 nm laser, we find a spectral evolution similar to the one measured in dark conditions (Figure 2a and 2b). Similar to the reaction in the dark, the longitudinal and transverse plasmon resonances blue shift by ~25 nm and ~3 nm, respectively, along with an increase in extinction (see also Supplementary S3). TEM images after 24 h also exhibit similar silver shell growth as in the dark (Supplementary S3).

On the contrary, during 24 h illumination with the 532 nm laser, the *in situ* extinction measurements display remarkable spectral changes when compared to the experiments in the dark and under 730 nm irradiation (Figure 2c). The longitudinal plasmon resonance initially blue shifts from 743 nm to 721 nm in 2 h, followed by a 14 nm red shift of the resonance in the next 5 h, and then again a blue shift of 65 nm at the end of 24 h. The transverse resonance also blue shifts by 15 nm along with the appearance of a new peak at ~420 nm (see also Supplementary S3).

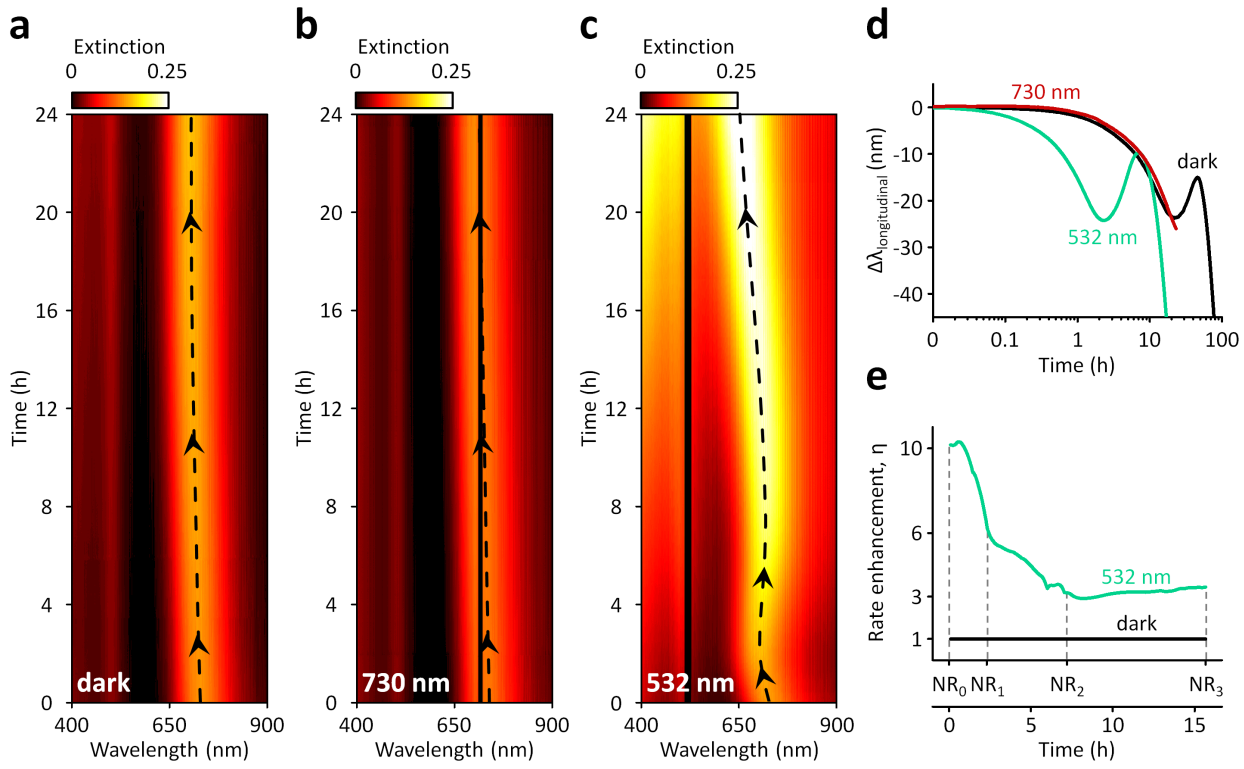

Figure 2. Core@shell growth under illumination. (**a**, **b**, **c**) Time evolution of the extinction spectra of Au@Ag core@shell nanorods over a period of 24 h under (**a**) dark conditions, (**b**) 55 mW 730 nm laser illumination, and (**c**) 240 mW 532 nm laser illumination. The black vertical lines in panels **b** and **c** correspond to the laser wavelengths which are blocked by notch filters. The black dashed lines indicate the shift in plasmon resonances with time. (**d**) Time evolution of the longitudinal plasmon resonance under different illumination conditions. (**e**) Rate enhancement of silver shell growth under 240 mW 532 nm (green) illumination compared to the experiment in dark, plotted as a function of the reaction time under 532 nm illumination.

We assess the growth kinetics by tracking the changes in the longitudinal plasmon resonance during the experiments in the dark and under 532 nm and 730 nm illuminations (Figure 2d). The similar growth kinetics for the 730 nm illumination and the dark experiments show that no

significant plasmon-driven silver shell growth occurs under these illumination conditions. Strikingly, the spectral changes under 532 nm illumination over a period of 24 h and under dark conditions over a period of 76 h are very similar, indicating a similar reaction pathway, albeit with a rate of spectral changes that is significantly faster for the 532 nm illumination experiment.

To quantify such rate enhancement, η, we first find the time, t_{dark}, at which a certain LSPR wavelength is reached in the dark. We then find the time, t_{532nm}, at which the same LSPR wavelength is reached under 532 nm illumination (Supplementary S4). From these values, we define the rate enhancement as $\eta = \partial t_{dark}/\partial t_{532nm}$ (Figure 2e). We observe an initial tenfold rate enhancement that quickly decreases and stabilizes to roughly a threefold enhancement at growth stage NR_2, corresponding to a silver shell thickness of ~4 nm.

In the following sections we will show how the observed large rate enhancement under 532 nm irradiation can be unequivocally attributed to the generation of hot holes in the gold cores *via* interband transitions, and to which extent other plasmonic activation mechanisms are contributing to the photochemical rate.

Photothermal effects

The non-radiative decay of LSPRs leads to local temperature increases on the gold nanorod surface, ΔT_{local}, which under cw irradiation can be quantified using:[15,32]

$$\Delta T_{local} = \frac{\sigma_{abs} I}{4\pi\beta\kappa R_{eq}} \quad \#(1)$$

where σ_{abs} is the absorption cross-section of the nanorod, I is the illumination intensity (optical power per unit area), β is the thermal capacitance coefficient of a nanorod, κ is the thermal conductivity of the surrounding medium, and R_{eq} is the radius of a sphere equivalent to

the volume of the nanorod. Under our laser intensities, we calculate that localized photothermal effects are negligible with $\Delta T_{local} \approx$ 1 - 3 milliKelvin (Supplementary S5).

The simultaneous illumination of a large number of nanoparticles in ensemble experiments, however, can lead to the rise of non-localized, macroscopic collective heating effects accompanied by large temperature gradients and non-trivial heat transport *via* conduction and convection. These collective photothermal effects can be several orders of magnitude larger than the localized ones and could in principle increase our reaction temperature by tens of Kelvins.[20,26,33,34] In our experiments, however, the power absorbed inside the reaction volume is the same under 532 nm and 730 nm illumination (Supplementary S2) and similar photothermal effects will therefore be generated in both irradiation experiments. As plasmonic enhancements are only observed for 532 nm illumination and not for 730 nm illuminations, we can confidently eliminate the contributions of photothermal effects in our silver shell growth.

Moreover, infrared camera and thermocouple measurements on the nanoparticle suspensions under plasmon excitation reveal experimental temperature increases in the reaction volume smaller than 1 K (Supplementary S5). Such a low temperature rise, which is corroborated by numerical modeling of the heat propagation inside the reaction volume (Supplementary S5), cannot explain the observed tenfold increase in the reaction rate.

Near-field enhancement

After ruling out any photothermal contribution to the silver shell growth, we investigate the effect of near-field enhancements using FDTD simulations. We calculate the electric field enhancement generated under 532 nm excitation using a three-dimensional electric field monitor around Au and Au@Ag nanorods corresponding to the four growth stages identified

experimentally (Figure 3a). To avoid artefacts due to a finite mesh size at the nanoparticle surface, we calculate the average near-field enhancement, $\langle NFE \rangle$, at distances between 0.5 nm to 10 nm away from the nanoparticle surface (see Supplementary S6 for details) using:

$$\langle NFE \rangle = \frac{1}{V} \iiint_{0.5\ \mathrm{nm}<r<10\ \mathrm{nm}} \frac{|\vec{E}|^2}{|\vec{E}_0|^2} \mathrm{d}V \quad \#(2)$$

where V is the integrated volume, r is the distance from a mesh cell outside of the nanorod to the nanorod surface, $\vec{E}$ is the electric field, and $\vec{E}_0$ is the incident field. The calculated average near-field enhancement at the nanorod surface increases with the silver shell growth, as shown in Figure 3b. The time evolution of $\langle NFE \rangle$ is in sharp contrast with the experimentally measured decrease in rate enhancement over the course of the reaction (Figure 3b, bottom panel), allowing us to rule out the role of near-fields as the dominant contributor to our plasmon-driven reaction.

Hot charge carriers

The absence of any plasmonic rate enhancement for silver shell growth under 730 nm illumination (Figure 2d) indicates that the generated intraband carriers are not sufficiently energetic to activate the core@shell growth. The carriers generated under 532 nm illumination, however, are able to significantly influence the reaction rate (Figure 2e). Partially thermalized hot carriers have energies close to the Fermi level, with the electron temperature of the thermalized distribution being mainly determined by the total absorbed optical power and not by the excitation wavelength.[35,36] The reaction rates observed under different illumination wavelengths therefore suggest that the main driving force behind the enhancement under 532 nm illumination is due to non-thermalized (first generation) carriers. To investigate the role of interband and intraband charge carriers generated under 532 nm illumination, we calculate the

power absorbed inside the nanorods at different stages of the silver shell growth using FDTD simulations (Figure 3c). Carriers generated in the sp-band of gold, *i.e.* intraband electrons, intraband holes, and interband electrons have high carrier velocities and typical mean free paths (MFPs) of 10 – 40 nm.[28] As these MFPs are similar to the nanorod size, all of these carriers could potentially contribute to the growth of the silver shell. Interband holes in the d-band, however, have significantly lower carrier velocities and MFPs typically smaller than 5 nm.[28] To discriminate the role of interband and intraband charge carriers, we therefore compare the observed rate enhancement with the total power absorbed inside the nanorod and the power absorbed within 4 nm from the nanorod surface for the different silver shell growth stages (Figure 3d).

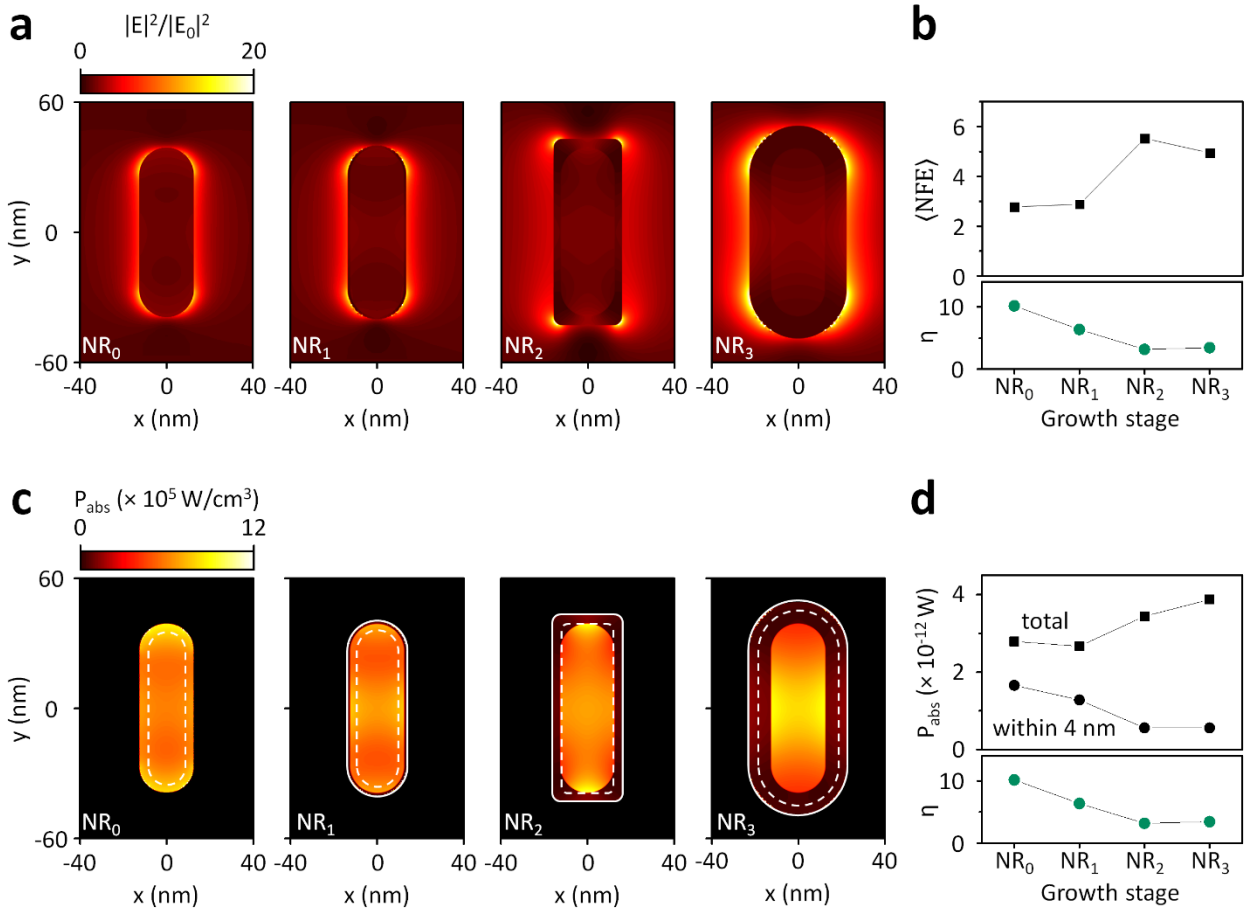

Figure 3. Near fields and hot charge carrier contributions. (**a**) 2D slices of the FDTD calculated electric field enhancements monitored at the center of the Au@Ag core@shell nanorods visualized at different silver shell growth stages corresponding to NR_0, NR_1, NR_2 and NR_3, under 532 nm illumination. (**b**) (top panel) Average near-field enhancement, $\langle NFE \rangle$, calculated by integrating the electric field intensities between distances of 0.5 nm and 10 nm from the nanoparticle surface at different silver shell growth stages. (**c**) 2D slices of the FDTD calculated absorbed power distribution monitored at the center of the core@shell nanorod at different silver shell growth stages, under 532 nm illumination. The white solid lines depict the boundaries of the core@shell nanorod and the white dashed lines correspond to a distance of 4 nm inwards from the nanorod surface. (**d**) (top panel) Total power absorbed (black squares) and

power absorbed inside a 4 nm range inwards from the nanorod surface (black circles) under our experimental laser intensity plotted as a function of the silver shell growth stage. The bottom panels in Figure 3b and 3d correspond to the experimentally measured plasmonic rate enhancement at different silver shell growth stages under 532 nm illumination, extracted from the full time evolution shown in Figure 2e. The lines connecting the symbols in Figure 3b and 3d are guides to the eye.

The total power absorbed inside the nanorod under 532 nm illumination (Figure 3d, black squares) increases with increasing silver shell growth. The power absorbed within 4 nm from the nanorod surface (Figure 3d, black circles), however, decreases with increasing silver shell thickness. In our light-driven synthesis under 532 nm irradiation, the measured plasmonic rate enhancement decreases roughly 3× from the growth stage NR_0 to NR_2 (see Figure 2e or bottom panels in Figure 3b and 3d), which is quantitatively similar to the trend calculated for power absorbed within 4 nm from the nanorod surface (Figure 3d). This agreement strongly implies that the experimentally observed plasmonic enhancement has to be attributed to charge carriers with an MFP of ~4 nm, *i.e.* hot d-band holes generated in the plasmonic gold cores. This interpretation is also consistent with the low losses in silver at 532 nm,[37] which result in carriers being primarily generated in gold. Such photogenerated carriers have to travel through the silver shell in order to perform redox reactions at the nanorod surface, which increases their recombination probability as the silver shell grows beyond a few nanometers in thickness.

The silver shell growth reaction involves the reduction of silver ions and the oxidation of ascorbic acid at the surface of the metal nanoparticles. However, the drastic decrease of plasmonic rate enhancement when the silver shell thickness approaches a value comparable to the mean free path of d-band holes (~4 nm) indicates that the consumption of holes by ascorbic

acid is the rate-limiting step of the plasmon-driven process.[5,17,35,38] Note that no silver shell growth is observed in a control experiment under 532 nm irradiation in the absence of ascorbic acid. Our results can therefore be interpreted in the framework of a reduced activation barrier for ascorbic acid oxidation under 532 nm illumination as compared to the reaction in the dark or under 730 nm illumination (Figure 4).[39] Under 730 nm laser irradiation, only intraband absorption can occur and the photon energy (= 1.70 eV) will be on average evenly distributed between short-lived, hot electrons and holes with mild reducing and oxidizing potentials.[35] Upon 532 nm irradiation, however, the photon energy (= 2.33 eV) is preferentially absorbed via interband transitions giving rise to a larger fraction of hot holes with high chemical potentials and therefore lower activation energies towards the oxidation of ascorbic acid.[19,35]

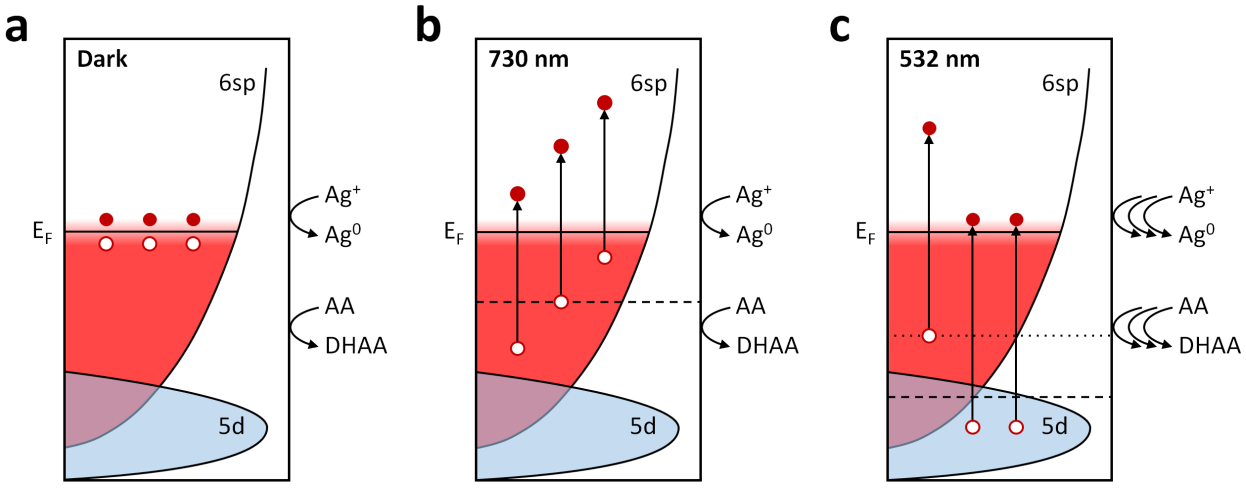

Figure 4. Hot hole-assisted silver shell growth. Schematic representation of the energy levels for the plasmon-driven oxidation of ascorbic acid (AA) to dehydroascorbic acid (DHAA) and the concomitant reduction of Ag^+ to Ag^0 on gold nanorods under (**a**) dark conditions, (**b**) 730 nm illumination, and (**c**) 532 nm illumination. The red and white circles denote electrons and holes respectively. The dashed lines in panel **b** and **c** represent the average energy of non-thermalized

holes under plasmon excitation. The dotted line in panel **c** represents the average energy of non-thermalized intraband holes, which are the only ones contributing to the plasmon-enhanced reactivity for shell thicknesses >4 nm.

A lower but still significant residual rate enhancement of ~3× with respect to the dark is observed at the growth stages NR_2 and NR_3, which points to the role of non-thermalized intraband hot holes, characterized by a relatively high potential energy (dotted line in Figure 4c) and long mean free paths. Ab initio calculations for 20 nm radius gold nanospheres (equivalent to the volume of our gold nanorods) have previously shown that, under 532 nm illumination, the amount of generated interband carriers is twice the amount of intraband ones.[19] In our experiments, while both interband and intraband holes contribute to the silver shell growth in the beginning (NR_0), only intraband holes can reach the nanorod surface and drive the oxidation of ascorbic acid when the silver shell thickness grows above ~4 nm (NR_3). By comparing the plasmonic rate enhancement at the growth stages NR_0 and NR_3, and by considering that only intraband holes contribute at NR_3, we find an approximate ratio of 2-to-1 interband-to-intraband contribution, in qualitative agreement with theoretical predictions.

Single-particle studies confirm the role of interband holes

Thanks to their high chemical potentials, non-thermalized (first generation) carriers in metal nanoparticles are the major contributors to plasmon-driven charge injection in photodetection and photocatalytic processes.[18] The angular distribution of these charge carriers strongly depends on their photogeneration mechanism, with interband charge carriers being uniformly distributed inside the nanoparticles and intraband charge carriers closely following the polarization of the incident light.[29] Such angular dependence suggests an alternative method to distinguish hot

charge carrier processes driven by interband and intraband transition events. Here we use the same photo-chemistry used in our ensemble nanorod experiments to study the spatial profile of laser-driven silver shell growth, by measuring the dark-field scattering spectra of several individual Au@Ag core@shell nanospheres grown under polarized laser excitation. We choose spheres over nanorods for single particle measurements as it is challenging to follow the transverse plasmon resonance of nanorods, due to their extremely low scattering cross-sections. Furthermore, the use of spherical gold nanoparticles ensures a homogeneous surface chemistry and allows us to compare orthogonal laser polarizations without adjusting for the different longitudinal and transverse absorption cross-sections of a nanorod. Briefly, a dilute suspension of 66 nm gold nanospheres is drop casted on a glass slide and allowed to dry, followed by the assembly of a flow cell around the nanoparticles using a glass slide and epoxy glue. The flow cell is then mounted on to a dark-field microscope (Figure 5a), where the scattering spectra of single nanoparticles are measured before and after their laser irradiation (see Methods). A silver growth solution is injected in to the flow cell, followed by 532 nm cw laser illumination of several nanoparticles at an intensity of 166 W/cm^2. The spectral sensitivity of our dark-field setup allows us to detect spectral shifts down to ~1 nm, corresponding to a silver shell thickness variation of ~2 Å. In our experiments, the laser intensity is chosen so as to generate negligible local temperature increases of ~60 milliKelvin and collective heating effects of ~0.1 K (Supplementary S7). Several experiments are performed by varying the illumination times from 5 min to 6 h.

In Figure 5b, we plot the measured plasmon resonance of a typical single gold nanoparticle before and after silver shell growth. After laser irradiation, the plasmon resonance blue shifts by 17 nm indicating the formation of a ~4 nm silver shell according to Mie theory calculations

(Supplementary S8). No silver growth is observed in the absence of laser irradiation or in the absence of gold nanoparticles, confirming the plasmonic contribution to the silver shell growth (Supplementary S9). To investigate the morphology of the core@shell nanoparticles, we place a polarizer in the dark-field scattering pathway of the nanoparticles (Figure 5a). By measuring the plasmon resonance of the nanoparticle before and after illumination at polarizations parallel and orthogonal to the laser polarization, we can estimate the silver shell growth along different directions. We find similar LSPR blue shifts at orthogonal polarizations indicating that the light-induced Au@Ag core@shell nanoparticle growth is isotropic (Figure 5c). We compare this isotropic growth to Monte Carlo simulations of the angular distribution of non-thermalized carriers reaching the nanoparticle surface (see Methods and Supplementary S10). In this model we generate carriers with a spatial distribution proportional to the absorbed power and we assign a propagation direction to each carrier. The propagation length follows an exponential distribution with the mean free path as the characteristic length. The propagation angle follows the predicted distributions for interband or intraband carriers.[18,29] We only evaluate carriers that reach the nanoparticle surface ballistically, by neglecting scattering at the nanoparticle surface and with other carriers. Carriers generated *via* intraband transitions have $\cos^2\theta$ and $|\cos^3\theta|$ contributions in their angular distribution, as they are accelerated along the direction of the optical field.[18,29] Here, θ is the angle between the laser polarization vector and the carrier propagation vector. This angular dependence is reflected in the angular distribution of hot carriers reaching the surface (Figure 5d). Conversely, carriers generated *via* interband transitions have an isotropic angular distribution, as the wavevector of the field does not appear in the matrix element of the Hamiltonian describing the transition.[18,29] This lack of angular dependency results in an isotropic distribution of hot carriers reaching the surface (Figure 5e). The

observation of isotropic silver shell growth therefore suggests that the reduction of Ag^+ ions is not directly driven by non-thermalized intraband electrons.

Furthermore, by grouping the experimentally measured resonance shifts according to the illumination time, we find that the silver shell growth occurs predominantly between 0 – 2 h, and that further growth is negligible at longer time scales (Figure 5c). An average blue shift of 16 ± 5 nm is observed after 6 h of illumination, suggesting a growth of 3.5 ± 1 nm silver shell around the gold nanospheres, according to Mie calculations. Similar to our bulk experiments, in which plasmonic enhancement is quenched after the growth of a ~4 nm shell, the suppression of silver shell growth after 4 nm thicknesses also points to the quenching of d-band holes reaching the nanoparticle surface, due to their extremely short mean free path.

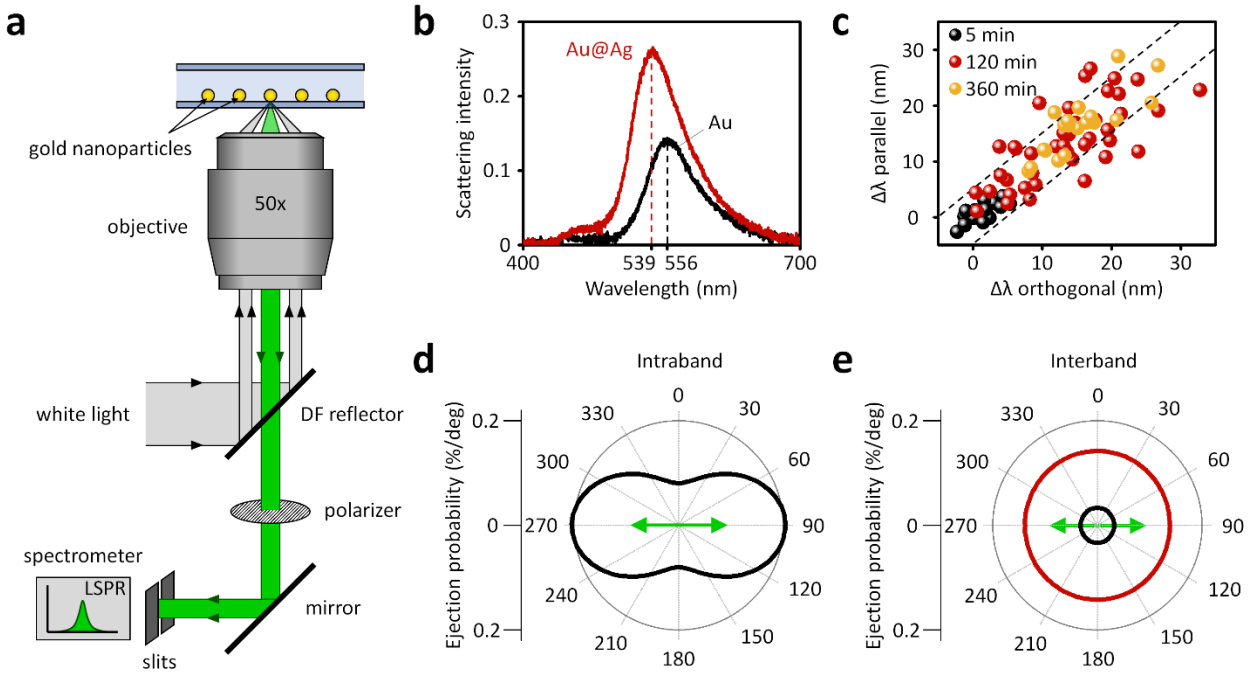

Figure 5. Spatial profile of hot charge carriers in single nanoparticles. (**a**) Illustration of the dark-field microscope used for single-particle studies of light-driven Au@Ag core@shell nanosphere synthesis. (**b**) Dark-field scattering spectra of a single gold nanoparticle (black curve) and corresponding Au@Ag core@shell nanoparticle (red curve) synthesized under 532 nm laser illumination. (**c**) Measured LSPR blue shift of several Au@Ag core@shell nanoparticles at polarizations parallel and perpendicular to the laser polarization. The blue shifts are measured from experiments with three different illumination periods of 5 min (black circles), 120 min (red circles), and 360 min (yellow circles). The dashed lines correspond to a difference of silver shell thickness of ± 1 nm at the orthogonal polarizations. (**d**, **e**) Calculated polar plots displaying the spatial ejection probability of (**d**) intraband (MFP = 30 nm for both electrons and holes) and (**e**) interband (MFP = 30 nm for electrons and 5 nm for holes) charge carriers. The red and black lines represent the spatial profile of electrons and holes respectively. The green arrow represents the laser polarization.

In summary, we have designed a light-driven Au@Ag core@shell nanoparticle synthesis in which all mechanisms of plasmon activation can be independently assessed. By proper choice of the illumination conditions and by accurate characterization and modeling of the structural, optical, and thermal properties of our growing core@shell nanoparticles, we exclude photothermal and near-field effects and identify d-band holes in gold as the main driving force behind the silver shell growth. Single-particle studies corroborate our conclusions from ensemble experiments, showing a quickly decreasing reaction rate with increasing shell thickness and isotropic silver growth under polarized illumination. Despite the low reduction potential of silver ions, our experiments suggest that plasmonic electrons in gold nanoparticles under 532 nm irradiation are able reduce silver ions only after the corresponding holes have been scavenged through the oxidation of ascorbic acid. Although in our plasmon-driven reaction, both interband carriers and in minor part intraband carriers contribute to the silver shell growth, the relative weight of these activation mechanisms is, in general, strongly dependent on the chemical properties of the species involved, including their reduction and oxidation potentials, their binding energies to the metal catalysts, and the evolving surface chemistry of the growing nanoparticle. Our strategy of combining an accurate choice of illumination parameters with detailed numerical modeling of the irradiated plasmonic nanostructures can be extended to the study of a variety of plasmon-driven processes in which several mechanisms simultaneously contribute to the observed reaction rate, from nanoparticle syntheses, to heterogeneous photocatalysis, and photothermal drug delivery.

ASSOCIATED CONTENT

Supporting Information

Supplementary Materials is uploaded as a separate file. It includes information on experimental details, morphological and optical characterization of Au & Au@Ag core@shell nanorods, modeling photon propagation in our reaction volume, *ex situ* extinction measurements and morphological characterization under different illumination conditions at t = 0 h and 24 h, evaluating plasmonic rate enhancement, thermal characterization under laser illumination, quantifying near-field enhancements, temperature calculations in single-particle studies, Mie theory calculations for the growth of Au@Ag core@shell nanospheres, control experiments to confirm the plasmonic nature of silver shell growth, and Monte Carlo simulations of hot carrier propagation.

AUTHOR INFORMATION

Rifat Kamarudheen (Email: r.kamarudheen@differ.nl, Twitter handle: @Rifat_Nano)

Guus J. W. Aalbers (Email: gjw.aalbers@gmail.com)

Ruben F. Hamans (Email: r.f.hamans@differ.nl, Twitter handle: @ruben_hamans)

Leon P. J. Kamp (Email: l.p.j.kamp@tue.nl)

Andrea Baldi (Email: a.baldi@vu.nl, Twitter handle: @calippoebbira)

Research group webpage: https://www.differ.nl/research/nea

Notes

The authors declare no competing financial interest.

ACKNOWLEDGMENT

We are grateful for the insightful feedback received from Dr. Ferry Nugroho (DIFFER), Dr. Eitan Oksenberg (AMOLF), and Dr. Sven Askes (AMOLF). This work was supported by the Netherlands Organisation for Scientific Research (NWO). Andrea Baldi and Ruben F. Hamans acknowledge support *via* the NWO Vidi award 680-47-550.

References

(1) Li, C.; Cao, Q.; Wang, F.; Xiao, Y.; Li, Y.; Delaunay, J.-J.; Zhu, H. Engineering Graphene and TMDs Based van Der Waals Heterostructures for Photovoltaic and Photoelectrochemical Solar Energy Conversion. *Chem. Soc. Rev.* **2018**, *47* (13), 4981–5037. https://doi.org/10.1039/C8CS00067K.

(2) Srituravanich, W.; Fang, N.; Sun, C.; Luo, Q.; Zhang, X. Plasmonic Nanolithography. *Nano Lett.* **2004**, *4* (6), 1085–1088. https://doi.org/10.1021/nl049573q.

(3) Wadell, C.; Syrenova, S.; Langhammer, C. Plasmonic Hydrogen Sensing with Nanostructured Metal Hydrides. *ACS Nano* **2014**, *8* (12), 11925–11940. https://doi.org/10.1021/nn505804f.

(4) Anikeeva, P.; Deisseroth, K. Photothermal Genetic Engineering. *ACS Nano* **2012**, *6* (9), 7548–7552. https://doi.org/10.1021/nn3039287.

(5) Langille, M. R.; Personick, M. L.; Mirkin, C. A. Plasmon-Mediated Syntheses of Metallic

Nanostructures. *Angew. Chemie - Int. Ed.* **2013**, *52* (52), 13910–13940. https://doi.org/10.1002/anie.201301875.

(6) Aslam, U.; Rao, V. G.; Chavez, S.; Linic, S. Catalytic Conversion of Solar to Chemical Energy on Plasmonic Metal Nanostructures. *Nat. Catal.* **2018**, *1* (9), 656–665. https://doi.org/10.1038/s41929-018-0138-x.

(7) Marimuthu, A.; Zhang, J.; Linic, S. Tuning Selectivity in Propylene Epoxidation by Plasmon Mediated Photo-Switching of Cu Oxidation State. *Science* **2013**, *339* (6127), 1590–1593.

(8) Zhang, X.; Li, X.; Zhang, D.; Su, N. Q.; Yang, W.; Everitt, H. O.; Liu, J. Product Selectivity in Plasmonic Photocatalysis for Carbon Dioxide Hydrogenation. *Nat. Commun.* **2017**, *8*, 14542.

(9) Jin, R.; Cao, Y.; Mirkin, C. A.; Kelly, K. L.; Schatz, G. C.; Zheng, J. G. Photoinduced Conversion of Silver Nanospheres to Nanoprisms. *Science* **2001**, *294* (5548), 1901–1903.

(10) Zhai, Y.; DuChene, J. S.; Wang, Y.-C.; Qiu, J.; Johnston-Peck, A. C.; You, B.; Guo, W.; DiCiaccio, B.; Qian, K.; Zhao, E. W.; et al. Polyvinylpyrrolidone-Induced Anisotropic Growth of Gold Nanoprisms in Plasmon-Driven Synthesis. *Nat. Mater.* **2016**, *15* (8), 889–895. https://doi.org/10.1038/nmat4683.

(11) Kim, Y.; Smith, J. G.; Jain, P. K. Harvesting Multiple Electron–Hole Pairs Generated through Plasmonic Excitation of Au Nanoparticles. *Nat. Chem.* **2018**, *10* (7), 763–769. https://doi.org/10.1038/s41557-018-0054-3.

(12) Brongersma, M. L.; Halas, N. J.; Nordlander, P. Plasmon-Induced Hot Carrier Science and

Technology. *Nat. Nanotechnol.* **2015**, *10* (1), 25–34. https://doi.org/10.1038/nnano.2014.311.

(13) Baffou, G.; Quidant, R. Nanoplasmonics for Chemistry. *Chem. Soc. Rev.* **2014**, *43* (11), 3898–3907. https://doi.org/10.1039/C3CS60364D.

(14) Ueno, K.; Juodkazis, S.; Shibuya, T.; Yokota, Y.; Mizeikis, V.; Sasaki, K.; Misawa, H. Nanoparticle Plasmon-Assisted Two-Photon Polymerization Induced by Incoherent Excitation Source. *J. Am. Chem. Soc.* **2008**, *130* (22), 6928–6929. https://doi.org/10.1021/ja801262r.

(15) Baffou, G.; Quidant, R. Thermo-Plasmonics: Using Metallic Nanostructures as Nano-Sources of Heat. *Laser and Photonics Reviews*. 2013, pp 171–187. https://doi.org/10.1002/lpor.201200003.

(16) Zhang, Y.; He, S.; Guo, W.; Hu, Y.; Huang, J.; Mulcahy, J. R.; Wei, W. D. Surface-Plasmon-Driven Hot Electron Photochemistry. *Chem. Rev.* **2018**, *118* (6), 2927–2954. https://doi.org/10.1021/acs.chemrev.7b00430.

(17) Zhao, J.; Nguyen, S. C.; Ye, R.; Ye, B.; Weller, H.; Somorjai, G. A.; Alivisatos, A. P.; Toste, F. D. A Comparison of Photocatalytic Activities of Gold Nanoparticles Following Plasmonic and Interband Excitation and a Strategy for Harnessing Interband Hot Carriers for Solution Phase Photocatalysis. *ACS Cent. Sci.* **2017**, *3* (5), 482–488. https://doi.org/10.1021/acscentsci.7b00122.

(18) Khurgin, J. B. Hot Carriers Generated by Plasmons: Where Are They Generated and Where Do They Go from There? *Faraday Discuss.* **2019**, *214* (0), 35–58.

https://doi.org/10.1039/C8FD00200B.

(19) Brown, A. M.; Sundararaman, R.; Narang, P.; Goddard, W. A.; Atwater, H. A. Nonradiative Plasmon Decay and Hot Carrier Dynamics: Effects of Phonons, Surfaces, and Geometry. *ACS Nano* **2016**, *10* (1), 957–966. https://doi.org/10.1021/acsnano.5b06199.

(20) Kamarudheen, R.; Castellanos, G. W.; Kamp, L. P. J.; Clercx, H. J. H.; Baldi, A. Quantifying Photothermal and Hot Charge Carrier Effects in Plasmon-Driven Nanoparticle Syntheses. *ACS Nano* **2018**, *12* (8), 8447–8455. https://doi.org/10.1021/acsnano.8b03929.

(21) Zhou, L.; Swearer, D. F.; Zhang, C.; Robatjazi, H.; Zhao, H.; Henderson, L.; Dong, L.; Christopher, P.; Carter, E. A.; Nordlander, P.; et al. Quantifying Hot Carrier and Thermal Contributions in Plasmonic Photocatalysis. *Science* **2018**, *362* (6410), 69–72. https://doi.org/10.1126/science.aat6967.

(22) Yu, Y.; Williams, J. D.; Willets, K. A. Quantifying Photothermal Heating at Plasmonic Nanoparticles by Scanning Electrochemical Microscopy. *Faraday Discuss.* **2018**, *210* (0), 29–39. https://doi.org/10.1039/C8FD00057C.

(23) Dubi, Y.; Sivan, Y. "Hot" Electrons in Metallic Nanostructures—Non-Thermal Carriers or Heating? *Light Sci. Appl.* **2019**, *8* (1), 89. https://doi.org/10.1038/s41377-019-0199-x.

(24) Jain, P. K. Taking the Heat Off of Plasmonic Chemistry. *J. Phys. Chem. C* **2019**, *123* (40), 24347–24351. https://doi.org/10.1021/acs.jpcc.9b08143.

(25) Christopher, P.; Xin, H.; Linic, S. Visible-Light-Enhanced Catalytic Oxidation Reactions

on Plasmonic Silver Nanostructures. *Nat Chem* **2011**, *3* (6), 467–472.

(26) Hogan, N. J.; Urban, A. S.; Ayala-Orozco, C.; Pimpinelli, A.; Nordlander, P.; Halas, N. J. Nanoparticles Heat through Light Localization. *Nano Lett.* **2014**, *14* (8), 4640–4645. https://doi.org/10.1021/nl5016975.

(27) Christensen, N. E.; Seraphin, B. O. Relativistic Band Calculation and the Optical Properties of Gold. *Phys. Rev. B* **1971**, *4* (10), 3321–3344. https://doi.org/10.1103/PhysRevB.4.3321.

(28) Bernardi, M.; Mustafa, J.; Neaton, J. B.; Louie, S. G. Theory and Computation of Hot Carriers Generated by Surface Plasmon Polaritons in Noble Metals. *Nat. Commun.* **2015**, *6* (1), 7044. https://doi.org/10.1038/ncomms8044.

(29) Khurgin, J. B. Fundamental Limits of Hot Carrier Injection from Metal in Nanoplasmonics. *Nanophotonics* **2020**, *9* (2), 453–471. https://doi.org/https://doi.org/10.1515/nanoph-2019-0396.

(30) Ye, X.; Jin, L.; Caglayan, H.; Chen, J.; Xing, G.; Zheng, C.; Doan-Nguyen, V.; Kang, Y.; Engheta, N.; Kagan, C. R.; et al. Improved Size-Tunable Synthesis of Monodisperse Gold Nanorods through the Use of Aromatic Additives. *ACS Nano* **2012**, *6* (3), 2804–2817. https://doi.org/10.1021/nn300315j.

(31) Rodríguez-González, B.; Burrows, A.; Watanabe, M.; Kiely, C. J.; Liz Marzán, L. M. Multishell Bimetallic AuAg Nanoparticles: Synthesis, Structure and Optical Properties. *J. Mater. Chem.* **2005**, *15* (17), 1755–1759. https://doi.org/10.1039/B500556F.

(32) Baffou, G.; Quidant, R.; Garcia de Abajo, F. J. Nanoscale Control of Optical Heating in

Complex Plasmonic Systems. *ACS Nano* **2010**, *4*, 709–716.

(33) Richardson, H. H.; Carlson, M. T.; Tandler, P. J.; Hernandez, P.; Govorov, A. O. Experimental and Theoretical Studies of Light-to-Heat Conversion and Collective Heating Effects in Metal Nanoparticle Solution. *Nano Lett.* **2009**, *9* (3), 1139–1146. https://doi.org/10.1021/nl8036905.Experimental.

(34) Baffou, G.; Berto, P.; Bermudez Urena, E.; Quidant, R.; Monneret, S.; Polleux, J.; Rigneault, H. Photoinduced Heating of Nanoparticle Arrays. *ACS Nano* **2013**, *7* (8), 6478–6488. https://doi.org/10.1021/nn401924n.

(35) Al-Zubeidi, A.; Hoener, B. S.; Collins, S. S. E.; Wang, W.; Kirchner, S. R.; Hosseini Jebeli, S. A.; Joplin, A.; Chang, W.-S.; Link, S.; Landes, C. F. Hot Holes Assist Plasmonic Nanoelectrode Dissolution. *Nano Lett.* **2019**, *19* (2), 1301–1306. https://doi.org/10.1021/acs.nanolett.8b04894.

(36) Jermyn, A. S.; Tagliabue, G.; Atwater, H. A.; Goddard, W. A.; Narang, P.; Sundararaman, R. Transport of Hot Carriers in Plasmonic Nanostructures. *Phys. Rev. Mater.* **2019**, *3* (7), 75201. https://doi.org/10.1103/PhysRevMaterials.3.075201.

(37) Yang, H. U.; D'Archangel, J.; Sundheimer, M. L.; Tucker, E.; Boreman, G. D.; Raschke, M. B. Optical Dielectric Function of Silver. *Phys. Rev. B* **2015**, *91* (23), 235137. https://doi.org/10.1103/PhysRevB.91.235137.

(38) Guo, W.; Johnston-Peck, A. C.; Zhang, Y.; Hu, Y.; Huang, J.; Wei, W. D. Cooperation of Hot Holes and Surface Adsorbates in Plasmon-Driven Anisotropic Growth of Gold Nanostars. *J. Am. Chem. Soc.* **2020**. https://doi.org/10.1021/jacs.0c03342.

(39) Kim, Y.; Dumett Torres, D.; Jain, P. K. Activation Energies of Plasmonic Catalysts. *Nano Lett*. **2016**, *16* (5), 3399–3407. https://doi.org/10.1021/acs.nanolett.6b01373.